Journal of Nanotechnology & Advanced Materials
An International Journal

http://dx.doi.org/10.18576/jnam/130102

Characterization of ZnO Nanoparticles Synthesized by Citrate Sol-gel Using Different Techniques

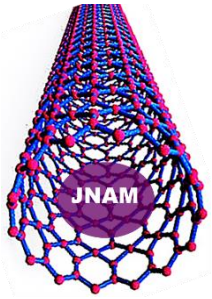

Emad A. Badawi[1,], H. Ibrahim[1], M. Abdel-Rahman[1], A. Ashour[1,2] and Essmat M. Hassan[3]*

[1] Department of Physics, Faculty of Science, Minia University, Minia City, 61519, Egypt.
[2] Department of Physics, Faculty of Science, Islamic University, Medina, Kingdom of Saudi Arabia.
[3] Department of Physics, Faculty of Science Aswan University, Aswan -81528, Egypt.

Received: 23 Oct. 2024, Revised: 1 Dec. 2024, Accepted: 30 Dec. 2024
Published online: 1 Jan. 2025.

Abstract: In this study we discussed crystal structure, crystallite size, lattice parameters and micro-strain, as well as defect and dislocation density of ZnO NPs are investigated using X-rays diffraction (XRD) and positron annihilation Doppler broadening energy spectroscopy (DBES). ZnO NPs size and elemental composition are studied using scanning electron microscopy (SEM) and energy dispersive X-ray analysis (EDX), respectively.

XRD microstructure characterization of ZnO NPs carried out using both **Williamson-Hall** and **Rietveld methods**, as well as anisotropic size-strain model (**Popa rules model**), is reported. The correlation between microstructural properties and DBES line-shape parameters at different chelating agent concentrations is also examined. Many defects/dislocations are observed at low chelating agent concentrations. Zn vacancies are identified as the major type of defects existing in our samples. Crystallite plot using Popa rules model revealed that crystallites at intermediate chelating agent concentrations are more isotropic, with clear spherical symmetry around optimum nucleation conditions. Good agreement between SEM estimated ZnO NPs size and XRD calculated crystallite size is observed around optimum nucleation conditions.

Keywords: ZnO Nanoparticles; Citrate Route Sol-gel Method; XRD Microstructure Characterization; Crystallite Size; Defect and Dislocation Density; Positron Annihilation Line-Shape Identification.

1. Introduction

ZnO is a group II-VI semiconductor with a wide bandgap (~ 3.37 eV at room temperature)[1], large exciton binding energy (~ 60 meV), high electron mobility, and high refractive index. It can sustain high temperature, large electric fields, and high-power operation [2,3]. It has wide applications and presented in different composition such as ZnO core-shell heterojunction by Chen et al [4]; Ga_2O_3/ZnO nanoparticle heterojunction by Met et al., [5]; Zno-Ga_2O_3 heterostructures by B. Zhao et. al, [6] and, ZnO thin film by Dogan et. al .,[7]. Owing to such unique properties, it is employed in light-emitting diodes, field-effect transistors, solar cells, UV lasers, gas sensors, UV photodetectors, piezoelectric transducers, antibacterial and UV protection, as well as many other biomedical and optoelectronic applications [3,8–13]. Furthermore, ZnO nanostructures have been studied extensively due to their enhanced performance over bulk ZnO, their chemical and thermal stability, their catalytic and anti-corrosion properties, as well as their optical and electrical properties that are size dependent [14–18].

Recently works are seen addressing ZnO (NPs) in biomedical applications such as cancer cell imaging. Zinc oxide nanoparticles focus on recent applications and advances in biomedical applications, toxicity studies, and antimicrobial studies. Additionally, the obstruction caused to the cellular processes leads to oxidative exertion, DNA damage, apoptosis, and proinflammatory effects [19–25]. Srivastav et al., indicated that ZnO NPs at low doses can act as a seed priming agent, to achieve better germination and seedling growth [23]. Khan et al., investigated that ZnO NPs accelerated ROS generation and reduced the antioxidant defense system in rice [21].

Research on the improvements of ZnO NPs properties have improved in the last few years. Numerous studies have reported its use as an antimicrobial agent [26–29], in sensors [30,31] and in energy cells [32]; Novel applications of ZnO NPs in biomedical engineering is also an emerging field of study with ZnONPs been applied for tissue regeneration, implant coatings, bio imaging, wound healing, development of cancer therapies, among others [26,32]. for photocatalysis [33].

In general, ZnO (NPs) have strong restrained effects versus malignant cells due to their ingrained toxicity, which they attain via causing intracellular ROS generation and tonic the apoptotic signaling pathway, making them an appropriate choice for anticancer remedy. Furthermore, when used as medicine carriers, ZnO (NPs) have been used to increase the medicines therapeutic bioavailability or biomolecules, giving an improvement for the therapy efficiency [19].

*Corresponding author e-mail: emad.badawi@mu.edu.eg

Several synthesis techniques of nanostructured ZnO have been investigated, as example beam molecular epitaxy, metal–organic vapor chemical deposition, sputtering, sol gel, laser pulsed deposition, hydrothermal, and mechanical milling [3,11–18]. Among all these mentioned techniques, sol gel is considered one of the best methods to grow metal oxide nanoparticles (NPs), such as ZnO NPs, because of its simplicity, reliability, reproducibility, and cost effectiveness [13–15,34–38]. Citric acid, which is an efficient agent of chelating, is considered one of the most widely used organic molecules in the sol-gel synthesis method. In this citrate route method, the citric acid is unsettled with a hydrous metal salt and the prepared mixed sol is warmed up till forming a Gel or viscous solution. When that gel is heated, the organic component burns at ~ 250 – 300 °C. Milling and then annealing the resulting powder produce the metal oxide NPs. During the sol-gel synthesis process, citric acid acts as ions of metal chelating agent as well as an organic fuel through the calcination process [39].

Crystal defects in ZnO NPs, such as impurity, point defects, dislocations, etc. have a strong effect upon their mechanical and optoelectronic properties. The control of such defects is crucial in material synthesis [15]. Therefore, a study of the effect of sol gel synthesis conditions on crystal defects of ZnO (NPs) are imperative. In the present work, a comprehensive study of the chelating agent effect on the crystal defects of synthesized ZnO (NPs) by citrate sol gel method is presented. ZnO (NPs) are synthesized using citric acid anhydrous ($C_6H_8O_7$) as a chelating agent and zinc acetate ($Zn(CH_3COO)_2.2H_2O$) as a source of zinc.

The effect of anhydrous citric acid has been studied thoroughly in the presented work to find the optimum conditions for ZnO (NPs) synthesis with the maximum purity and minimum size. The effect of chelating agent on the crystal structure, the crystallite size, the lattice micro-strain, defects, and the dislocation density of ZnO (NPs) is studied utlizing X-rays diffraction (XRD) and Doppler broadening spectroscopy technique based on positron annihilation interaction. Microstructure characterization of synthesized ZnO NPs has been carried out using both Williamson-Hall [40] and Rietveld [41] methods. Crystallite size, micro-strain, and lattice parameters are also studied using anisotropic size-strain model (Popa rules model [42]).

Positron annihilation technique is a non-destructive powerful technique used for material characterization. It is widely applied in the microstructure studies of metal alloys, semiconductors, and polymers [43–47]. It gives advantageous information concerning the defects nature of ZnO NPs [18,38,48]. DBES (Doppler broadening energy spectroscopy) of the electron–positron annihilation radiation is described with two different line-shape parameters (S-parameters and W-parameters) which are sensitive to microstructural changes [49]. The correlation between microstructural properties and line-shape parameters of positron annihilation DBES at various anhydrous citric acid concentrations is investigated. In addition, ZnO NPs size and elemental composition are studied using energy dispersive X-ray (EDX) analysis and scanning electron microscopy (SEM), respectively.

2. Experimental Details

2.1 Synthesis of ZnO NPs

The chemical reagents are used from analytical grade (Techno Pharma Chem). They were applied as received from the producer without extra refinement. Chemical reagents were dissolved with de-ionized water (50 ml) to prepare the aqueous solutions as needed. ZnO (NPs) preparation by citrate route method is achieved using 0.09 M of zinc acetate dihydrate: $Zn(C_4H_6O_4)_2.2H_2O$ as zinc source mixed with different concentrations (0.025 M – 0.2 M) of anhydrous citric acid (H_3Cit or $C_6H_8O_7$) which serves as chelating agent. Then, to remove the excess water, the mix is heated for one hour at 80 °C. During continued heating, at temperature 120 °C, the solution turns more to viscous and ultimately becomes a xerogel, that is again heated for another one hour at 250 °C for completely drying. The obtained powder is a precursor, which is milled and then heat treated (calcined) in a boat of ceramic at 600 °C for 2 hours, then cooling down until room temperature is achieved and the ZnO desired is produced.

Chemical Reaction Mechanism

Citric acid (H_3Cit) is a weak organic acid, which ionizes in water in 3 steps represented by the following equations [50]:

$$H_3Cit + H_2O \rightleftharpoons H_2Cit^- + H_3O^+ \quad (1)$$

$$H_2Cit^- + H_2O \rightleftharpoons HCit^{2-} + H_3O^+ \quad (2)$$

$$HCit^{2-} + H_2O \rightleftharpoons Cit^{3-} + H_3O^+ \quad (3)$$

The formation of metal citrate complexes is extremely affected by the molar ratio, temperature, concentration, and reactants of pH. It is the potential to prepare complexes with specified structures by control of the reaction conditions. A zinc citrate complex in polymeric form, $[Zn(H_2Cit)(H_2O)]_n$, is usually formed at low pH [51]:

$$Zn^{2+} + H_3Cit + H_2O \rightleftharpoons [Zn(H_2Cit)(H_2O)]_n \quad (4)$$

Thermal decomposition of the zinc citrate complex leads to the forming of zinc oxide [52].

2.2 Measurements and Characterization

2.2. 1 X-ray Diffraction (XRD)

XRD characterization was obtained using X-ray unit (JEOL) with Model JSDX-60PA. This model is equipped with a Cukα-radiation of wavelength λ equal 0.15412 nm. The applied source of X-ray uses 40 kV and 35 mA for operation. Samples were scanned from 20° to 90° with a continuous rate of slow scanning (1° min^{-1}) and a small time constant (1 sec).

2.2.2 SEM and EDX

ZnO (NPs) Size and elemental composition were determined utilizing JEOL SEM (JSM – IT 200) at 25 kV voltage of operation.

2.2.3 Positron Annihilation Doppler Broadening Technique

The positrons and electrons electromagnetic interaction increases the possibility of $e^+ - e^-$ pairs annihilation. In such case, the pair annihilation energy is transferred to electromagnetic radiation quanta (two-annihilation γ photons):

$$e^+ + e^- \longrightarrow \gamma_1 + \gamma_2 \quad (5)$$

In the e^+e^- pair center of mass frame, the annihilation photons energy is the same as the electron rest energy and positron, $E_0 = m_0c^2$ = 511 keV. In this case, the two emitted γ photons are in opposite directions [43,46,47]. DBES technique is utilized to probe ZnO samples at the Positron Science Laboratory. DBES spectra were measured with approximately 2500 cps counting rate utilizing detector of HPGe (Ortec type with efficiency of 35% and 1.5 keV resolution at an annihilation peak of 511 keV). The samples of DBES were taken at room temperature, after being pressed into pellets. Each sample spectrum saved with total counts of 2.0 million.

The DBES spectra of samples were characterized into two line-shape parameters (S and W). The S-parameter is the integrated counts area A relative to the total counts (**see Fig. 1**). The used energy ranges from 510.3 to 511.7 keV (known as S width). The background is measured and subtracted from the measurements. The S-parameter is sensitive to the change of the positron states due to microstructural changes [49] and it indicates to the relative low momentum of the electron positron annihilation field. The W-parameter gives the high momentum part of the pair annihilation field. W-parameter is determined as an integrated counts area B relative to total counts (shown in **Fig. 1**). The used wings energy ranges are 508.0 to 509.4 keV (left W width) and 512.6 to 514.0 keV (right W width). The definition of S- and W-parameters from Doppler broadening is shown schematically in **Fig. 1**.

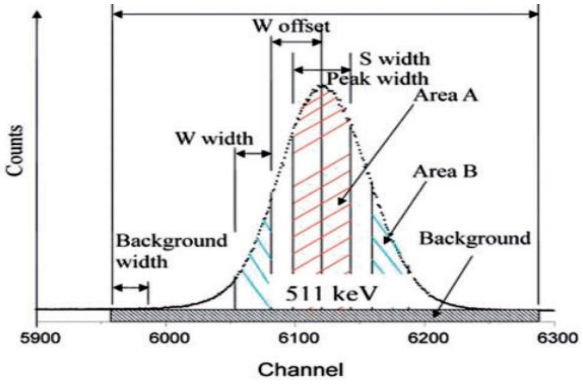

Fig. 1: DBES line-shape S- and W-parameters.

3. Results and Discussion

3.1 X-ray Diffraction

Fig. 2 shows patterns of XRD for prepared samples at various concentrations of anhydrous citric acid, ranging from 0 to 0.2 M. Apart from for the peak of diffraction at 2θ of 25°, all peaks could be indexed to a hexagonal wurtzite ZnO with a main (101) reflection and eight peaks with planes (100), (002), (102), (110), (103), (200), (112), and (201) are also observed [52]. In **Fig. 2**, the intensity of the peaks diffraction decreases with increasing the concentration of anhydrous citric acid from 0 to 0.2 M, as this leads to destroying crystal as the degree of crystallinity decrease. The first of observation marks is reduced the degree of crystallinity as a function of increasing anhydrous citric acid concentrations. Also appear a diffraction peak of graphene oxide (rGO) peak with increasing anhydrous citric acid. Resolved diffraction peaks of the (002) plane splitting. Observation of new splitting peaks in rGO1 and rGO2 as shown in **Fig. 2** at 2θ = 24.5° and 25.1° which agree with reference [53]. A small diffraction peak at 2θ of 47.8° is related to the (102) plane of rGO structure in [53]. Also, the same observation with our present work as shown in **Fig. 2** at 2θ=47.5°. The characteristic of the (002) planes discussed in more details [53–56] due to impurities of our samples.

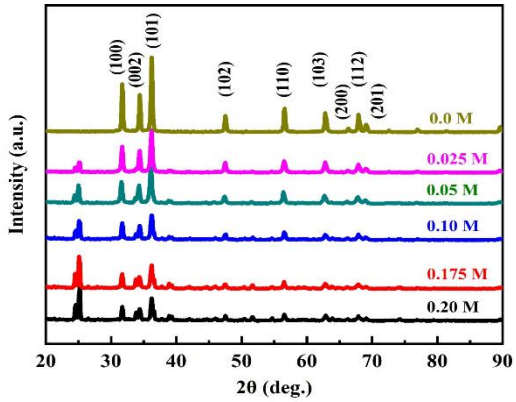

Fig. 2: XRD patterns of nanoparticles ZnO are synthesized at different citric acid concentrations

The XRD patterns of calcined samples of ZnO nanoparticles in the range of 2θ =20°to 90°are shown in **Fig. 2**. All evident peaks could be indexed as the ZnO wurtzite structure (JCPDS cards 38-0356,41-1359, JCPDS Data Card No: 36-1451). As shown in **Fig. 2**, this peak becomes less prominent as the concentration of anhydrous citric acid decreases and disappears completely in the absence of citric acid (without the presence of the organic matrix). XRD peaks related to carbon impurities that are reduced with increase of Zn acetate concentration have been previously reported for ZnO nanostructures synthesized using activated carbon [49]. Also, these samples considered to be monocrystalline due to splitting disappearing in the XRD peaks [50,51]. Traces of carbon have been detected in our samples using EDX analysis, as will be shown later in this work.

3.1.1 XRD Analysis Using Williamson-Hall (WH) Method

XRD analysis of peaks mainly depends on the peak profile and position in addition to the intensity of the peak. The shape of the peak is usually modeled with various functions like Gaussian, Cauchy, or a combination of functions such as (Voigt, pseudo-Voigt, or Pearson VII). Information such as parameters of shape, the position of the peak, and integral breadth is obtained. The mean crystallite size (D_c) and micro-strain (ε) of samples are estimated by applying the Williamson–Hall method [40]:

$$B\,cos\theta = K\,\lambda/D_c + 2\varepsilon\,sin\theta \qquad (6)$$

where D_c is the crystallite size mean, ε is the strain introduced inside samples, θ is the diffraction angle (Bragg angle), λ is the wavelength, K is a constant ($equal$ 0.89), and B is the full width at half maximum (FWHM). **Fig. 3** shows plots of Williamson-Hall (WH) assuming an isotropic nature of two ZnO samples with citric acid concentration 0.025 and 0.175.

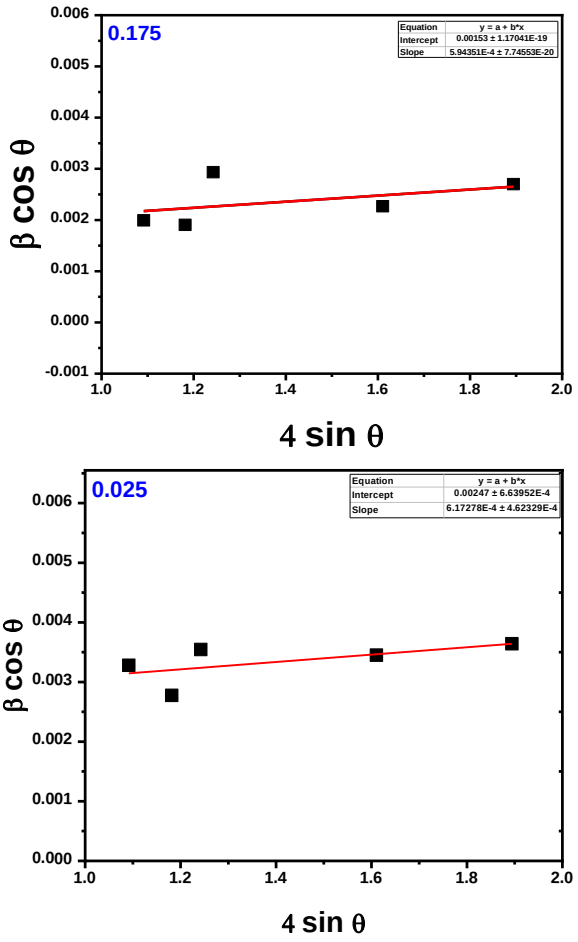

Fig. 3: plots of Williamson-Hall (WH) with an isotropic nature of two ZnO samples (Citric acid concentration 0.025and 0.175).

Instrumental contribution correction

The contribution of instrumental broadening must be considered to extract the intrinsic FWHM. In the case of instrumental and measured profiles following a function of Gaussian, the width of broadening for the diffraction intrinsic profile is estimated using this formula:

$$B_c = [(B_{exp})^2 - (B_i)^2]^{1/2} \qquad (7)$$

where B_c, B_{exp} and B_i are the width of broadening for the intrinsic (corrected), experimentally measured, and instrumental profiles, respectively.

The density of dislocation is expressed with the length per unit volume, ρ(cm^{-2}), is calculated from the r.m.s. value of micro-strain $\langle\varepsilon^2\rangle^{1/2}$ and the average value of the crystallite size D_c using the formula [57]:

$$\rho = \frac{3\sqrt{2\pi}\,\langle\varepsilon^2\rangle^{1/2}}{D_c b} \qquad (8)$$

where b is the Burgers vector of ZnO [58]. The defect density $\bar{\rho}(cm^{-3})$, the number of defect sites per unit volume, is calculated from dislocation density ρ(cm^{-2}) using the formula:

$$\rho(cm^{-2}) = \bar{\rho}(cm^{-3}) \cdot b \qquad (9)$$

The crystallite size, lattice micro-strain, dislocation, and defect density of synthesized ZnO NPs at anhydrous citric acid with different concentrations are summarized in Table 1 and **Fig. 4**. As shown in **Fig. 4(a)**, a maximum crystallite size with a value 129.3 nm is estimated at anhydrous citric acid equal zero. Then a fast decrease in the crystallite size when the citric acid concentration increases. A minimum crystallite size (44.4 nm) is found at 0.05 M of anhydrous citric acid. Moreover, an increase in concentration of citric acid gives an increase in crystallite size.

It should be noted that in all samples, zinc acetate concentration is fixed. In other words, increasing citric acid concentration increases citrate to zinc source ratio. Particle size dependence on citrate to metal source ratio has been previously reported for gold NPs synthesized using citrate-based reduction method [59]. Apparently, at small concentrations (< 0.025 M), citric acid is not sufficient to completely reduce the Zn precursor resulting in agglomeration of particles. However, excess concentrations of citrate ions (> 0.1 M) will decrease the number of reactive Zn^{2+} ions which, in turn, will result in a slow nucleation process due to the lack of zinc citrate complex formation (Eq. 4). This explains why optimum nucleation is observed around 0.025 M – 1.0 M of anhydrous citric acid, with smallest particle size of 44.4 nm obtained at 0.05 M concentration. It is worth noting that good agreement between SEM estimated particle size and XRD calculated crystallite size is observed around optimum nucleation conditions, as will be shown later in this work.

Lattice micro-strain as well as dislocation and defect densities, shown in **Fig. 4(b) – 4(d)**, are found to be sensitive to citric acid concentration at low values ($\leq 0.05\ M$). At higher concentrations, however, they tend to slightly decrease/saturate. Such behavior can be explained by considering the crystallite size dependence on citrate concentration shown in **Fig. 4 (a)**. At low concentration of citric acid, the crystallite size tends to decrease rapidly. Such a decrease in crystallite size results in an increase in grain boundary regions. These regions are highly defective in nature [18,48]. As a result, a large number of defects/dislocations are introduced due to this fast decrease of crystallite size at low citrate concentration. On the other hand, the afore mentioned slow nucleation process at higher concentrations of citrate ions (> 0.1 M) is believed to be responsible for the saturation observed in dislocation and defect densities.

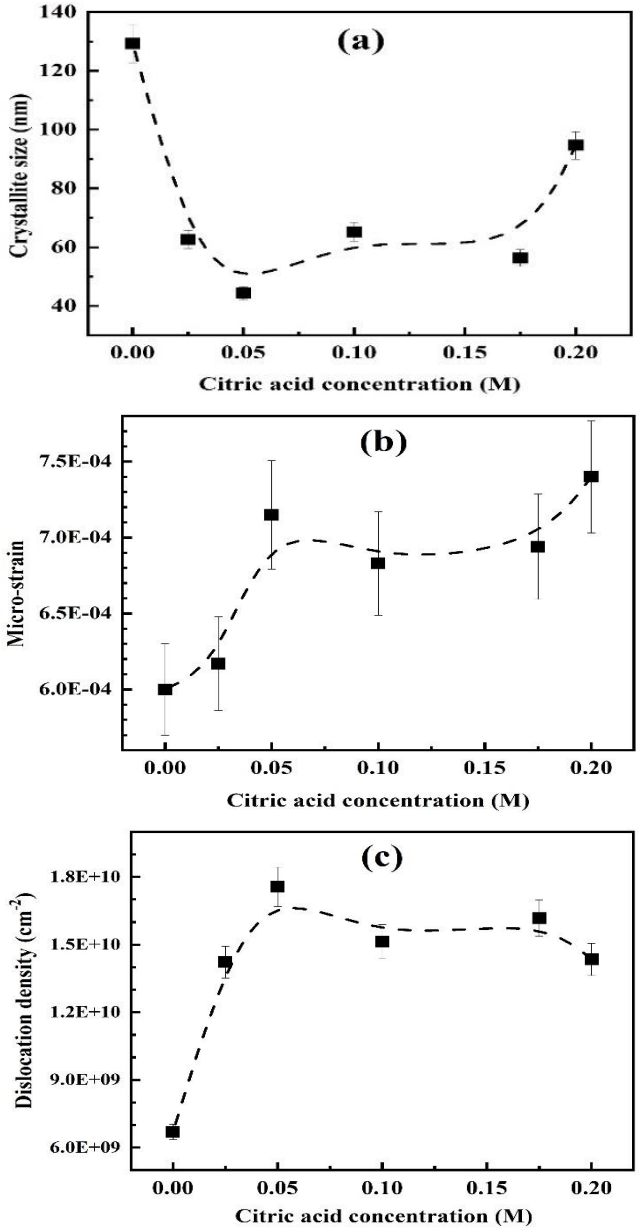

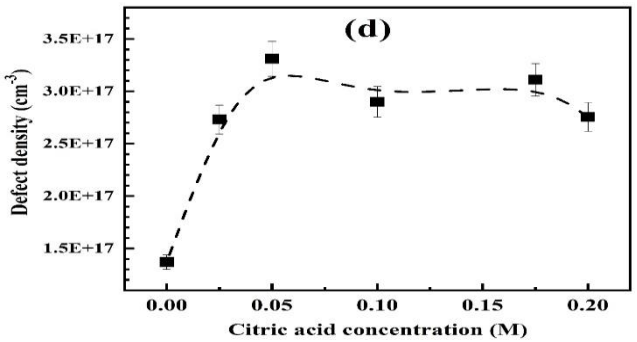

Fig. 4: Williamson-Hall XRD-calculated (a) crystallite size, (b) micro-strain, (c) dislocation density, and (d) defect density of the nanoparticles ZnO synthesized at different concentrations of citric acid.

3.1.2 Analysis Using Rietveld Method (MAUD Program)

3.1.2.1 Isotropic size-strain model

Lattice parameters, micro-strain, and crystallite size determined by analyzing XRD patterns using Rietveld software: Materials Analysis Using Diffraction (MAUD) program [60] are given in **Table 2**. Clearly, there is no noticeable change in cell parameters as the concentration of anhydrous citric acid increases. Furthermore, comparing values of crystallite size and micro-strain are presented in **Table 1** and **Table 2**, It is evident that crystallite size and micro-strain calculations using both Williamson-Hall and Rietveld methods are consistent and of the same order of magnitude.

Table 1: Crystallite size, lattice micro-strain, dislocation, and defect density estimated based on XRD using Williamson-Hall method.

Citric acid concentration (M)	Crystallite size (nm)	Micro-strain	Dislocation density (cm^{-2})	Defect density (cm^{-3})
0.000	129.25	6.00E-04	7.15E+09	1.37E+17
0.025	62.65	6.17E-04	1.42E+10	2.73E+17
0.050	44.40	7.15E-04	1.76E+10	3.31E+17
0.100	65.21	6.83E-04	1.51E+10	2.90E+17
0.175	56.33	6.94E-04	1.62E+10	3.11E+17
0.200	94.61	7.40E-04	1.43E+10	2.76E+17

Table 2: Lattice parameters, crystallite size, and micro-strain estimated based on XRD using Rietveld method (Isotropic size-strain model).

Citric acid concentration (M)	Lattice parameters (Å)		Crystallite size (nm)	Micro-strain
	A	C		
0.000	3.254	5.211	139.00	1.60E-4
0.025	3.256	5.215	63.35	6.24E-4
0.050	3.256	5.216	50.08	7.79E-4
0.100	3.254	5.215	66.21	5.37E-4
0.175	3.256	5.216	56.58	7.20E-4
0.200	3.254	5.211	93.05	9.59E-4

A fit MAUD obtained by applying isotropic model for the samples of ZnO is presented in **Fig. 5a**. The experimental

data are presented as points, and the MAUD fit presented by solid line. At the bottom, the difference pattern is presented, with a factor of reliability (R_w) equal 14.09%. **Fig**. 5b. reveals two samples, one is prepared using anhydrate citric acid while the second sample is prepared using monohydrated citric acid at the same molar ratio. The sample prepared using anhydrate citric acid is not pure although we can obtain the purity by decreasing the amount of citric acid as discussed and declared before in **Fig**. **5b**. The sample prepared using monohydrated citric acid is pure although the crystallite size obtained by anhydrate citric acid is smaller than that obtained by monohydrated citric acid. as will be discussed in the analysis of the XRD part. **Fig. 5b.** presents two samples, the first prepared with anhydrate citric acid and the second with monohydrated citric acid at the same molar ratio. The sample prepared with anhydrate citric acid was not pure, although purity can be obtained by decreasing the amount of citric acid (as discussed in the previous). Molar ratio of zinc acetate to citric acid (anhydrate citric acid or monohydrated citric acid) as shown in **Fig. 5b**. as following for both (anhydrous) and for (monohydrated) 0.0 M.

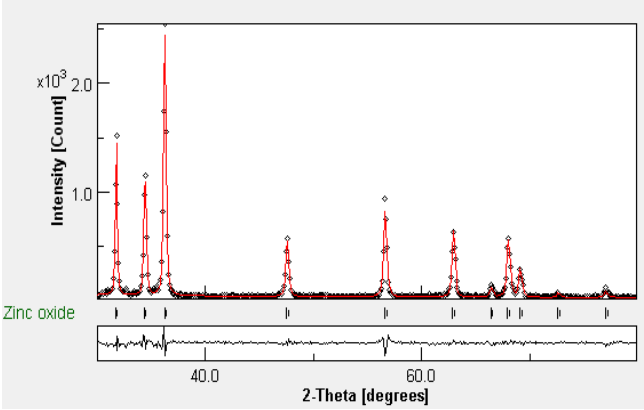

Fig. 5 a.

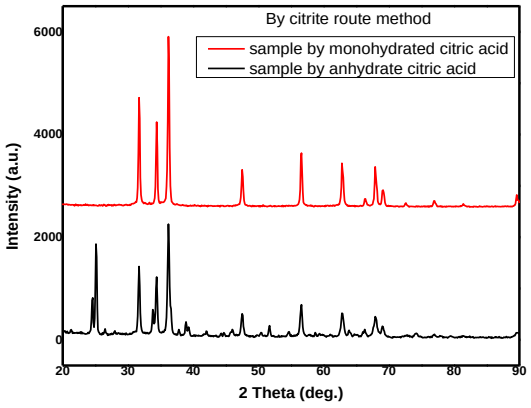

Fig. 5 b.

Fig. 5: (5a): A fit MAUD obtained utilizing isotropic model for the samples of ZnO. The experimental data are presented as points, and the fit MAUD as solid line. At the bottom, the difference pattern is presented, with factor of reliability (R_w) equals 14.09%.

(5b): XRD patterns of ZnO powders obtained at the same molar ratio 1.00: 1.00 by anhydrate and monohydrated citric acid respectively.

3.1.2.2 Anisotropic size-strain model (Popa rules model)

Lattice parameters, micro-strain, and crystallite size are further analyzed using anisotropic size-strain model (Popa rules model [42]). Calculated values are given in Table 3. Evidently, lattice parameters obtained are the same as in **Table 2**. Meanwhile, crystallite size and micro-strain calculations are consistent with isotropic size-strain model values except for very low and very high anhydrous citric acid concentrations. For better understanding of such deviation, especially in micro-strain values at these particular concentrations, crystallite plot using Popa rules model for different citric acid concentrations is shown in **Fig. 6**. Obviously, crystallites at very low and very high anhydrous citric acid concentrations are completely anisotropic, while crystallites at intermediate concentrations are more isotropic, with clear spherical symmetry around optimum nucleation conditions. As shown in **Fig. 6.** for 0.05 M and for 0.1 M citric acid concentrations seams as an optimum spherical than other concertation of citric acid is more isotropic.

Table 3: Lattice parameters, crystallite size, and micro-strain estimated based on XRD using Popa rules model.

Citric acid concentration (M)	Lattice parameters (Å)		Crystallite size (nm)	Micro-strain
	A	C		
0.000	3.254	5.211	98.47	2.76E-4
0.025	3.256	5.215	65.86	5.50E-4
0.050	3.256	5.216	50.71	6.15E-4
0.100	3.254	5.215	70.88	7.39E-4
0.175	3.256	5.216	58.71	9.49E-4
0.200	3.254	5.211	96.64	1.12E-3

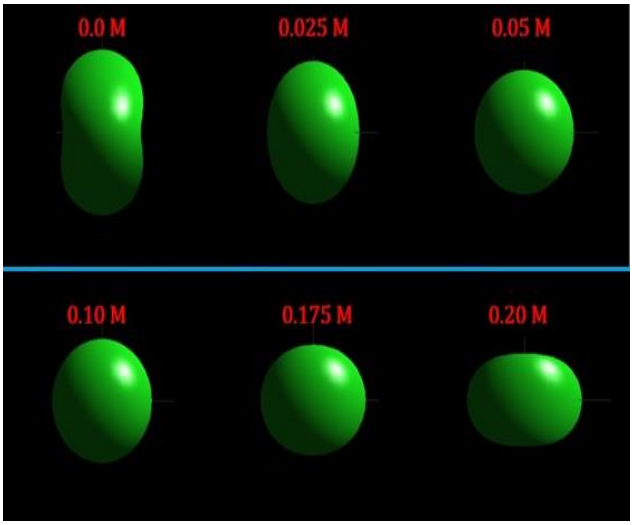

Fig. 6: Crystallite plot using Popa rules model for nanoparticles of ZnO synthesized at different concentrations of citric acid.

3.2 Positron Annihilation Doppler Broadening Measurements

The obtained DBES spectra of the electron – positron annihilation radiation is analyzed using the SP program. It is important to note that S-parameter is sensitive to annihilation with low momentum electrons. Positron annihilation with low momentum electrons takes place more frequently when defects concentration increases. As a result, more defects such as vacancies or voids in the material will cause an increase in the integrated counts between energy 510.3 and 511.7 keV (area A of **Fig. 1**), which in turn will increase the value of S-parameter. **Fig. 7** shows the spectrum for ZnO at 0.0 M of citric acid using Na^{22} positron source.

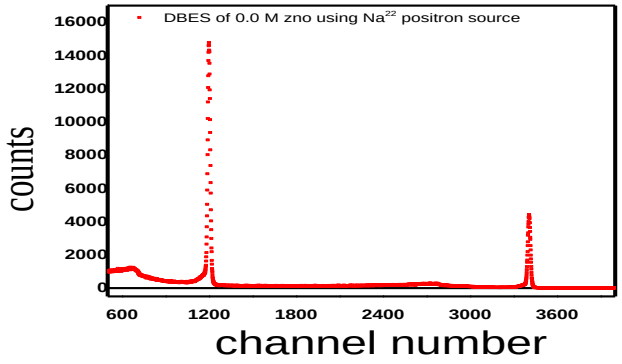

Fig. 7: DBES for ZnO nanoparticles synthesized 0.0 M of citric acid using Na^{22} positron source.

Fig. 8 shows the evaluated line-shape S- and W-parameters at different citric acid concentrations. As shown, S-parameter initially increases with increasing citric acid concentration and then, at higher citric acid concentrations, starts to decrease. This indicates an increase in defect densities at low citric acid concentration followed by a slight decrease of defects at higher concentrations, which corroborates our XRD analysis (**Fig. 5 c – d**). W-parameter which characterizes the positron annihilation with the high momentum electrons (annihilation with core electrons), however, has the reverse behavior of the S-parameter.

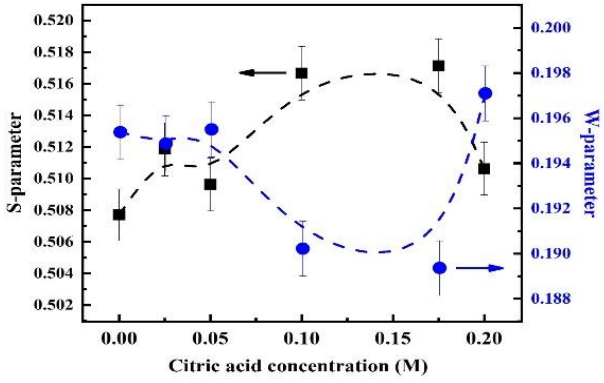

Fig. 8: Line-shape S- and W-parameters of nanoparticles ZnO synthesized at different concentrations of citric acid.

It is interesting to note that the behavior of the S-parameter as a function of citric acid concentration (**Fig. 8**) is almost opposite to that of ZnO crystallite size (**Fig. 5a**). To further verify this, the S-parameter is plotted versus the crystallite size (**Fig. 9**). The obtained results agree well with the findings of Dutta *et al.* [18]. This is maybe because decreasing crystallite size results in an increase in highly defective grain boundary regions, which in turn, will increase the value of S-parameter.

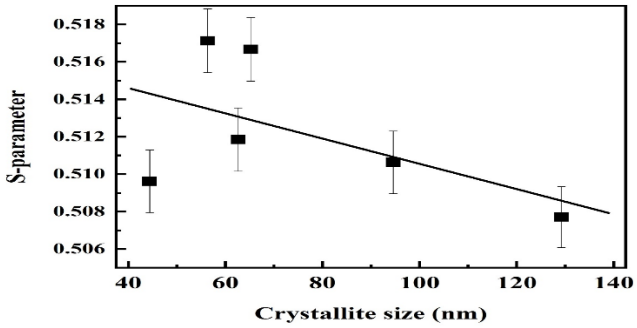

Fig. 9: S-parameter versus ZnO crystallite size.

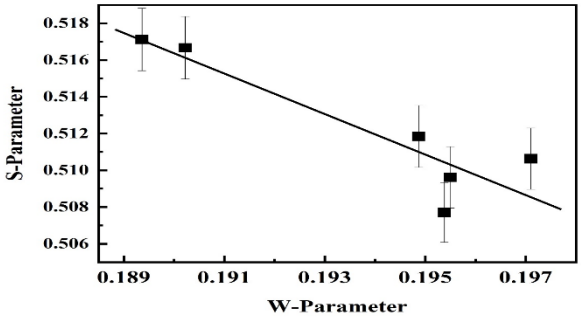

Fig. 10: S-parameter versus W-parameter for ZnO nanoparticles are synthesized at different citric acid concentrations

To identify the nature of the positron trapping sites (defects); the S-parameter is plotted versus W-parameter (**Fig. 10**). The linear relationship observed in **Fig. 10** indicates the presence of one major type of trapping sites in the system. In group II-VI semiconductors, such as ZnO, positron annihilation with the outer *d*-electrons of group II metals is dominant [61]. Therefore, in ZnO, positrons tend to annihilate more at Zn vacancies rather than oxygen vacancies. Considering this fact as well as the findings of **Fig. 10**, we believe that Zn vacancies are the major type of defects existing in our samples [61].

3.3 SEM Measurements and EDX analysis

SEM images **Fig. 11**, analyzed using ImageJ bundled with Java program used to estimate the average ZnO NPs size. The particle size distribution is estimated from the SEM images analyzed by the ImageJ program. The average nanoparticle size has been determined from the histogram. Also, we have found that, as a function of citric acid

concentration, particle size behaviors in the same manner as nano-crystallite size as shown in (**Fig. 5a**). **Fig. 11** shows SEM images for ZnO samples synthesized at citric acid concentration of 0.025 M and 0.2 M, respectively. The inset of **Fig. 11** represents the particle size distribution estimated from the SEM images analyzed by the ImageJ program. The average nanoparticle size has been determined from the histogram. We have found out that, as a function of citric acid concentration, particle size behaves in the same manner as nano-crystallite size (**Fig. 5a**).

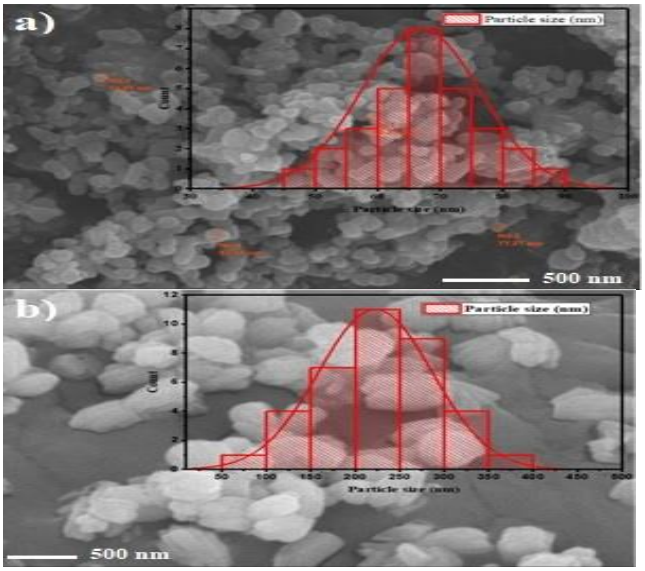

Fig. 11: SEM images of ZnO nanoparticles synthesized at a) 0.025 M and b) 0.2 M citric acid.

However, good agreement between estimated particle size and XRD calculated crystallite size is observed only around optimum nucleation conditions (small crystallite size). For example, at citric acid concentration of 0.025 M (**Fig. 11a**), the average particle size (66.84 nm) agrees well with the nano crystallite size calculated from the XRD analysis (62.65 nm using Williamson-Hall method and 63.35 nm using Rietveld method). In the meantime, away from such optimum conditions (at high citric acid concentration, > 0.1 M), significant differences are observed between estimated particle size and calculated crystallite size. At citric acid concentration of 0.2 M (**Fig. 11b**), for instance, the average particle size (222.66 nm) is much larger than the crystallite size calculated from the XRD analysis (94.61 nm using Williamson-Hall method and 93.05 nm using Rietveld method).

We believe that the slow nucleation process due to the lack of zinc citrate complex formation that takes place at high citric acid concentration is responsible for particles agglomeration which is the reason for the observed difference. It is worth noting that other researchers have previously reported differences between SEM/TEM estimated particle size and XRD calculated crystallite size in nanocrystalline ZnO synthesized via sol-gel and other chemical route methods [34,35,48]. Our results corroborate that XRD calculated crystallite size does not necessarily match the real nanoparticle size and should not be used solely to estimate the nanoparticle size. From the above results using different methods of XRD Williamson-Hall method, Rietveld method and Popa rules model with SEM it is clear the concentration of citric acid from 0.025 to 0.175 M have lower minimum 44.4 nm size to the maximum values of size about 70.88 nm. It is also we can realize that the optimum concentration of citric acid varies from 0.025 to 0.175 M as isotropic.

EDX spectroscopy of ZnO NPs synthesized at citric acid concentration of 0.025 M is shown in **Fig. 12**. In addition to zinc and oxygen, traces of carbon are detected as indicated by the small impurity peak observed near the origin at ~ 0.28 keV. This agrees with the diffraction peak detected at 2θ of 25° in the XRD patterns of **Fig. 2** [60], which, as previously explained, is related to impurities of graphitic carbon [53] formed from anhydrous citric acid after combustion during the ZnO NPs synthesis process [62,63].

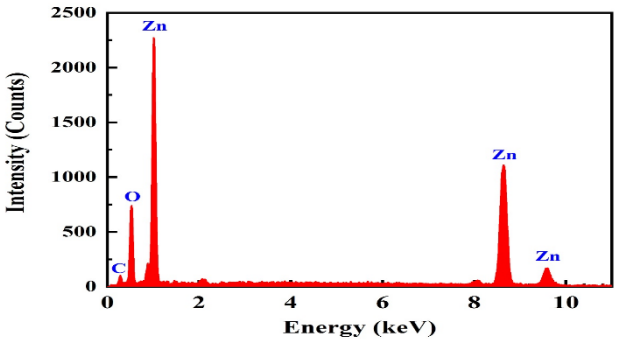

Fig. 12. EDX spectroscopy of nanoparticles ZnO synthesized at 0.025 M citric acid.

4. Conclusions

ZnO NPs are synthesized using anhydrous citric acid as a chelating/complexing agent and zinc acetate as zinc source. The effect of chelating agents has been studied thoroughly in this work in order to obtain the optimum conditions for ZnO NPs synthesis with maximum purity and minimum size. Increasing the concentration of zinc source, relative to the chelating agent, enhances crystallinity and purity of synthesized ZnO NPs. At small concentrations (< 0.025 M), citric acid is not sufficient to completely reduce the Zn precursor resulting in agglomeration of particles. On the other hand, excess concentrations of citrate ions (> 0.1 M) result in a slow nucleation process due to the lack of zinc citrate complex formation. Optimum nucleation is observed around 0.025 M – 1.0 M of anhydrous citric acid, with smallest particle size of 44.4 nm obtained at 0.05 M concentration. Good agreement between SEM estimated particle size and XRD calculated crystallite size is observed around optimum nucleation conditions. XRD analysis using Popa rules model shows that crystallites at very low and very

high chelating agent concentrations are anisotropic while crystallites at intermediate concentrations are more isotropic, with clear spherical symmetry around optimum nucleation conditions.

Many defects/dislocations are observed at low chelating agent concentrations followed by saturation/slight decrease of defects/dislocations density at higher chelating agent concentrations. The increase in defects/dislocations density at low concentration is attributed to the increase in the highly defective grain boundary regions due to the fast decrease of crystallite size at low citrate concentration. The slow nucleation process is believed to be the reason for the saturation observed at higher concentrations. The correlation between microstructural properties and DBES line-shape parameters at different chelating agent concentrations is confirmed. Zn vacancies are identified as the major type of defects existing in our samples. Also, from the results we can conclude that the optimum concentration of citric acid gives reliable values of crystallites size and micro stain analyses by three XRD methods. At low concertation of citric acid 0.0 M and high concertation of citric acid above 0.1 M crystallites at very low and very high anhydrous citric acid concentrations are completely anisotropic.

Acknowledgement

The authors wish to thank and have mercy on the spirit of the late Professor **M. R. Ebied** for his leadership of the group for using the different Methods of XRD analysis. Also, the authors pray to God about the late. The forgiven and his spirit present in every good work and effort.

References

[1] Ouyang W, Chen J, Shi Z and Fang X 2021 Self-powered UV photodetectors based on ZnO nanomaterials *Applied Physics Reviews* **8**, **031315** 1–28

[2] S.M.Sze and KWOK.K.NG 1995 *Physics of Semiconductor Devices* vol 3

[3] Özgür Ü D, Avrutin V and Morkoç H 2013 Zinc oxide materials and devices grown by MBE *Molecular Beam Epitaxy* pp 369–416

[4] Chen Y, Su L, Jiang M and Fang X 2022 Switch type PANI/ZnO core-shell microwire heterojunction for UV photodetection *Journal of Materials Science and Technology* **105** 259–65

[5] Mei T, Li S, Zhang S, Liu Y and Li P 2022 Simply equipped ε-Ga2O3 film/ZnO nanoparticle heterojunction for self-powered deep UV sensor *Physica Scripta* **97** 15808

[6] Zhao B, Wang F, Chen H, Zheng L, Su L, Zhao D and Fang X 2017 An Ultrahigh Responsivity (9.7 mA W−1) Self-Powered Solar-Blind Photodetector Based on Individual ZnO–Ga2O3 Heterostructures *Advanced Functional Materials* **27**, **170026** 1–8

[7] Doğan Ü, Sarcan F, Koç K K, Kuruoğlu F and Erol A 2022 Effects of annealing temperature on a ZnO thin film-based ultraviolet photodetector *Physica Scripta* **97** 15803

[8] Lupan O, Shishiyanu S, Ursaki V, Khallaf H, Chow L, Shishiyanu T, Sontea V, Monaico E and Railean S 2009 Synthesis of nanostructured Al-doped zinc oxide films on Si for solar cells applications *Solar Energy Materials and Solar Cells* **93** 1417–22

[9] Dong H, Zhou B, Li J, Zhan J and Zhang L 2017 Ultraviolet lasing behavior in ZnO optical microcavities *Journal of Materiomics* **3** 255–66

[10] Chai G Y, Lupan O, Rusu E V., Stratan G I, Ursaki V V., Sontea V, Khallaf H and Chow L 2012 Functionalized individual ZnO microwire for natural gas detection *Sensors and Actuators, A: Physical* **176** 64–71

[11] Liang S, Sheng H, Liu Y, Huo Z, Lu Y and Shen H 2001 ZnO Schottky ultraviolet photodetectors *Journal of Crystal Growth* **225** 110–3

[12] Hu Y C, Lee T H, Chang P Z and Su P C 2015 High power Co3O4/ZnO p-n type piezoelectric transducer *Thin Solid Films* **584** 112–5

[13] Ghamsari M S, Alamdari S, Han W and Park H H 2017 Impact of nanostructured thin ZnO film in ultraviolet protection *International Journal of Nanomedicine* **12** 207–16

[14] Alias S S, Ismail A B and Mohamad A A 2010 Effect of pH on ZnO nanoparticle properties synthesized by sol-gel centrifugation *Journal of Alloys and Compounds* **499** 231–7

[15] Eixenberger J E, Anders C B, Wada K, Reddy K M, Brown R J, Moreno-Ramirez J, Weltner A E, Karthik C, Tenne D A, Fologea D and Wingett D G 2019 Defect Engineering of ZnO Nanoparticles for Bioimaging Applications *ACS Applied Materials and Interfaces* **11** 24933–44

[16] Kawakami M, Hartanto A B, Nakata Y and Okada T 2003 Synthesis of ZnO nanorods by nanoparticle assisted pulsed-laser deposition *Japanese Journal of Applied Physics, Part 2: Letters* **42**

[17] Lupan O, Chow L, Ono L K, Cuenya B R, Chai G, Khallaf H, Park S and Schulte A 2010 Synthesis and characterization of ag- or sb-doped zno nanorods by a facile hydrothermal route *Journal of Physical Chemistry C* **114** 12401–8

[18] Dutta S, Chattopadhyay S, Sutradhar M, Sarkar A, Chakrabarti M, Sanyal D and Jana D 2007 Defects and the optical absorption in nanocrystalline ZnO *Journal of Physics: Condensed Matter* **19** 236218

[19] Anjum S, Hashim M, Malik S A, Khan M, Lorenzo J M, Abbasi B H and Hano C 2021 Recent advances in zinc oxide nanoparticles (Zno nps) for cancer diagnosis, target drug delivery, and treatment *Cancers* **13**

[20] Du J, Tang J, Xu S, Ge J, Dong Y, Li H and Jin M 2020 ZnO nanoparticles: recent advances in ecotoxicity and risk assessment *Drug and Chemical Toxicology* **43** 322–33

[21] Khan A R, Azhar W, Wu J, Ulhassan Z, Salam A, Zaidi S H R, Yang S, Song G and Gan Y 2021 Ethylene participates in zinc oxide nanoparticles induced biochemical, molecular and ultrastructural changes in rice seedlings *Ecotoxicology and Environmental Safety* **226** 112844

[22] Rajput V D, Minkina T, Fedorenko A, Chernikova N, Hassan T, Mandzhieva S, Sushkova S, Lysenko V, Soldatov M A and Burachevskaya M 2021 Effects of zinc oxide nanoparticles on physiological and anatomical indices in spring barley tissues *Nanomaterials* **11**

[23] Srivastav A, Ganjewala D, Singhal R K, Rajput V D, Minkina T, Voloshina M, Srivastava S and Shrivastava M 2021 Effect of zno nanoparticles on growth and biochemical responses of wheat and maize *Plants* **10**

[24] Jin M, Li N, Sheng W, Ji X, Liang X, Kong B, Yin P, Li Y, Zhang X and Liu K 2021 Toxicity of different zinc oxide nanomaterials and dose-dependent onset and development of Parkinson's disease-like symptoms induced by zinc oxide nanorods *Environment International* **146** 106179

[25] Rajeshkumar S, Lakshmi T and Naik P 2019 Recent advances and biomedical applications of zinc oxide nanoparticles *Green Synthesis, Characterization and Applications of Nanoparticles* 445–57

[26] Khatami M, Varma R S, Zafarnia N, Yaghoobi H, Sarani M and Kumar V G 2018 Applications of green synthesized Ag, ZnO and Ag/ZnO nanoparticles for making clinical antimicrobial wound-healing bandages *Sustainable Chemistry and Pharmacy* **10** 9–15

[27] Rad S S, Sani A M and Mohseni S 2019 Biosynthesis, characterization and antimicrobial activities of zinc oxide nanoparticles from leaf extract of Mentha pulegium (L.) *Microbial Pathogenesis* **131** 239–45

[28] Ginjupalli K, Alla R, Shaw T, Tellapragada C, Kumar Gupta L and Nagaraja Upadhya P 2018 Comparative evaluation of efficacy of Zinc oxide and Copper oxide nanoparticles as antimicrobial additives in alginate impression materials *Materials Today: Proceedings* **5** 16258–66

[29] Saravanan M, Gopinath V, Chaurasia M K, Syed A, Ameen F and Purushothaman N 2018 Green synthesis of anisotropic zinc oxide nanoparticles with antibacterial and cytofriendly properties *Microbial Pathogenesis* **115** 57–63

[30] Basha S K, Lakshmi K V and Kumari V S 2016 Ammonia sensor and antibacterial activities of green zinc oxide nanoparticles *Sensing and Bio-Sensing Research* **10** 34–40

[31] Arafat M M, Ong J Y and Haseeb A S M A 2018 Selectivity shifting behavior of Pd nanoparticles loaded zinc stannate/zinc oxide (Zn 2 SnO 4 /ZnO) nanowires sensors *Applied Surface Science* **435** 928–36

[32] Iqbal J, Abbasi B A, Mahmood T, Kanwal S, Ahmad R and Ashraf M 2019 Plant-extract mediated green approach for the synthesis of ZnONPs: Characterization and evaluation of cytotoxic, antimicrobial and antioxidant potentials *Journal of Molecular Structure* **1189** 315–27

[33] Roshitha S S, Mithra V, Saravanan V, Sadasivam S K and Gnanadesigan M 2019 Photocatalytic degradation of methylene blue and safranin dyes using chitosan zinc oxide nano-beads with Musa × paradisiaca L. pseudo stem *Bioresource Technology Reports* **5** 339–42

[34] Alwan R M, Kadhim Q A, Sahan K M, Ali R A, Mahdi R J, Kassim N A and Jassim A N 2015 Synthesis of Zinc Oxide Nanoparticles via Sol – Gel Route and Their Characterization *Nanoscience and Nanotechnology* **5** 1–6

[35] Zak A K, Abrishami M E, Majid W H A, Yousefi R and Hosseini S M 2011 Effects of annealing temperature on some structural and optical properties of ZnO nanoparticles prepared by a modified sol-gel combustion method *Ceramics International* **37** 393–8

[36] Omri K, Najeh I, Dhahri R, El Ghoul J and El Mir L 2014 Effects of temperature on the optical and electrical properties of ZnO nanoparticles synthesized by sol-gel method *Microelectronic Engineering* **128** 53–8

[37] Ciciliati M A, Silva M F, Fernandes D M, De Melo M A C, Hechenleitner A A W and Pineda E A G 2015 Fe-doped ZnO nanoparticles: Synthesis by a modified sol-gel method and characterization *Materials Letters* **159** 84–6

[38] Dutta S, Sarkar S and Ganguly B N 2013 Positron Annihilation Study of ZnO Nanoparticles Grown Under Folic Acid Template *Journal of Material Science & Engineering* **03** 1–8

[39] Wen W and Wu J M 2014 Nanomaterials via solution combustion synthesis: A step nearer to controllability *RSC Advances* **4** 58090–100

[40] Williamson G K and Hall W H 1953 X-ray line broadening from filed aluminium and wolfram *Acta Metallurgica* **1** 22–31

[41] Rietveld H M 1969 A profile refinement method for nuclear and magnetic structures *Journal of Applied Crystallography* **2** 65–71

[42] Popa N C 1998 The (hkl) Dependence of Diffraction-Line Broadening Caused by Strain and Size for all Laue Groups in Rietveld Refinement *Journal of Applied Crystallography* **31** 176–80

[43] Puska M J and Nieminen R M 1994 Theory of positrons in solids and on solid surfaces *Reviews of modern Physics* **66** 841

[44] Eldrup M and Singh B N 2000 Study of defect annealing behaviour in neutron irradiated Cu and Fe using positron annihilation and electrical conductivity *Journal of Nuclear Materials* **276** 269–77

[45] Slugeň V, Kuriplach J, Ballo P and Domonkoš P 2004 Hydrogen implantation effect in copper alloys selected for ITER investigated by positron annihilation spectroscopy *Nuclear Fusion* **44** 93–7

[46] Sundar C S and Viswanathan B 1996 Positron annihilation spectroscopy *Metals Materials and Processes* **8** 1–8

[47] Grafutin V I and Prokop'ev E P 2002 Positronic annihilation spectroscopy in material structure studies *Uspekhi Fizicheskikh Nauk* **172** 82–3

[48] Chakrabarti M, Jana D and Sanyal D 2013 Positron annihilation characterization of nanocrystalline ZnO *Vacuum* **87** 16–20

[49] Li Y, Zhang R, Chen H, Zhang J, Suzuki R, Ohdaira T, Feldstein M M and Jean Y C 2003 Depth profile of free volume in a mixture and copolymers of poly(N-vinyl-pyrrolidone) and poly(ethylene glycol) studied by positron annihilation spectroscopy *Biomacromolecules* **4** 1856–64

[50] Wyrzykowski D, Czupryniak J, Ossowski T and Chmurzyński L 2010 Thermodynamic interactions of the alkaline earth metal ions with citric acid *Journal of Thermal Analysis and Calorimetry* **102** 149–54

[51] Deng Y F and Zhou Z H 2009 Synthesis and crystal structure of a zinc citrate complex [Zn(H 2cit)(H 2O)] n *Journal of Coordination Chemistry* **62** 1484–91

[52] Farbun I A, Romanova I V., Terikovskaya T E, Dzanashvili D I and Kirillov S A 2007 Complex formation in the course of synthesis of zinc oxide from citrate solutions *Russian Journal of Applied Chemistry* **80** 1798–803

[53] Gupta B, Kumar N, Panda K, Kanan V and Joshi S 2017 Role of oxygen functional groups in reduced graphene oxide for lubrication *Nature Publishing Group* 1–14

[54] Nasrollahzadeh M S, Hadavifar M, Ghasemi S S and Arab Chamjangali M 2018 Synthesis of ZnO nanostructure using activated carbon for photocatalytic degradation of methyl orange from aqueous solutions *Applied Water Science* **8**

[55] Hasnidawani J N, Azlina H N, Norita H, Bonnia N N, Ratim S and Ali E S 2016 Synthesis of ZnO Nanostructures Using Sol-Gel Method *Procedia Chemistry* **19** 211–6

[56] Wójcik A, Kopalko K, Godlewski M, Łusakowska E, Paszkowicz W, Dybko K, Domagała J, Szczerbakow A and Kamińska E 2004 Monocrystalline and polycrystalline ZnO and ZnMnO films grown by atomic layer epitaxy - Growth and characterization *Acta Physica Polonica A* **105** 667–73

[57] Dini G, Ueji R, Najafizadeh A and Monir-vaghefi S M 2010 Flow stress analysis of TWIP steel via the XRD measurement of dislocation density *Materials Science & Engineering A* **527** 2759–63

[58] Singh A, Kumar D, Khanna P K, Kumar M and Prasad B 2013 Post annealing effect on structural and optical properties of ZnO thin films derived by sol-gel route *Journal of Materials Science: Materials in Electronics* **24** 4607–13

[59] Tyagi H, Kushwaha A, Kumar A and Aslam M 2016 A Facile pH Controlled Citrate-Based Reduction Method for Gold Nanoparticle Synthesis at Room Temperature *Nanoscale Research Letters* **11**

[60] Abdel-Rahman M, Ibrahim H, Mostafa M Y A, Abdel-Rahman M A, Ebied M R and Badawi E A 2021 The characterization of ZnO nanoparticles by applying x-ray diffraction and different methods of peak profile analysis *Physica Scripta* **96** 095704

[61] Sartiman S S, Djaja N F and Saleh R 2013 Chromium-Doped ZnO Nanoparticles Synthesized by Co-Precipitation: Chromium Effects *Materials Sciences and Applications* **04** 528–37

[62] H. Ibrahim, M. Abdel-Rahman, Hani Khallaf and Emad A. Badawi, J. Nanotech. & Adv. Mat. 12, No. 1, 1-11 (2024).

[63] E. A. Badawi, H. Ibrahim, M. R. Ebied, M. Abdel-Rahman, H. Khallaf, M. A. Abdel Rahman1, E. E. Assem, and A. Ashour, Int. J. Thin. Fil. Sci. Tec. 11, No. 3, 257-266 (2022).